Ceramics International 49 (2023) 24454–24468

Contents lists available at ScienceDirect

Ceramics International

journal homepage: www.elsevier.com/locate/ceramint

Investigation of quantum dot luminescent solar concentrator single, double and triple structures: A ray tracing simulation study

T.A. de Bruin, W.G.J.H.M. van Sark *

Utrecht University, Copernicus Institute of Sustainable Development, Princetonlaan 8a, 3584CB, Utrecht, The Netherlands

ARTICLE INFO

Keywords:
Photovoltaics
Nanoparticles
Device optimization
Energy harvesting window
Monte Carlo simulation
tandem LSC

ABSTRACT

Quantum dot based luminescent solar concentrators (QDLSCs) are a special class of transparent photovoltaics (TPV), especially suited for building integrated photovoltaics (BIPV). Photons are absorbed by luminescent species in a waveguide and emitted at a red-shifted wavelength. Due to total internal reflection, these photons are absorbed by the solar cells attached to the sides. Successful deployment requires high conversion efficiency and high transparency, which are contradictory requirements. We have performed Monte-Carlo ray tracing simulations to investigate single, double, and triple QDLSCs and have assessed their optical and electrical performance. To this end, eight different semiconductor quantum dot materials have been used with various absorption and emission properties, and Stokes' shift. Device efficiency is analyzed for different average visible transmission (AVT) values, thus considering the human photopic response. The range of luminescent quantum efficiencies (30%–70%) leads to maximum efficiency of 2% for a single QDLSC, 2.4% for a double, and 2.7% for a triple structure, at high transparency and good color rendering index. Further improvements are possible towards >5% at high transparency with near-unity quantum efficiencies.

1. Introduction

It is widely recognized that photovoltaic (PV) solar energy systems ranging from solar parks to residential roof-mounted systems will play a paramount role in the future energy system [1–3]. Besides the urgency to replace fossil fuel-based energy production, the world energy demand is expected to grow, with the built environment covering 50%–70% of total energy demand [1], also due to an increase in electric vehicle and heating deployment [4]. The need arises for energy generation technologies that are highly compatible with the built environment. Conventional crystalline silicon solar modules are often found on rooftops of residential and commercial buildings, which are selected for their orientation and unobstructed incoming solar irradiance. However, in city centers where tall buildings dominate, lack of horizontal roof space, shading effects, and an increase in diffuse irradiance lower the effectiveness of conventional PV modules [4,5].

In much of the literature, a proposed solution for PV in the urban environment is to develop PV components that are simultaneously an integral part of the building envelope, denoted as Building Integrated Photovoltaics (BIPV) [4–8]. Today, BIPV solutions are primarily available in a colored, opaque form on roofs and facades, while transparent BIPV solutions, such as in fully glazed high-rise buildings, are attracting attention. These BIPV solutions require optimization of transparency in relation to efficiency as the PV window has two functions, i.e., being transparent and generating electricity, hence the term transparent photovoltaics (TPV). Several technologies have been suggested to fulfill the role of BIPV windows. The Luminescent Solar Concentrator (LSC) is considered one of the most promising technologies due to its ability to selectively absorb (non-)visible light [9] and its low costs [10].

The operational principle of an LSC device is to absorb incoming light with a so-called luminophore species dispersed inside a transparent waveguide material that is part of the window, e.g., as a coating on window glass. After absorption, red-shifted light will be emitted isotropically by the luminophore. Based on the principle of total internal reflection, most of this emitted light can reach the sides of the window, where PV cells are attached to the window frame to convert the captured light into electricity. The refractive index of the waveguide determines this amount of emitted light, and for typical LSC waveguides, 75% can reach the sides.

The first LSC was proposed in 1977 by Goetzberger and Greubel [11] as a solution to reduce the cost of PV systems. However, their lasting popularity [5,9,12] is rather due to their flexibility in color [13] and shape [14,15] combined with excellent performance under diffuse irradiance during cloudy days [16–18].

For LSCs to be an important BIPV asset, their conversion efficiencies must be increased. Current power conversion efficiencies hover

* Corresponding author.
E-mail address: w.g.j.h.m.vansark@uu.nl (W.G.J.H.M. van Sark).

https://doi.org/10.1016/j.ceramint.2022.12.084
Received 31 August 2022; Received in revised form 9 December 2022; Accepted 10 December 2022
Available online 21 December 2022

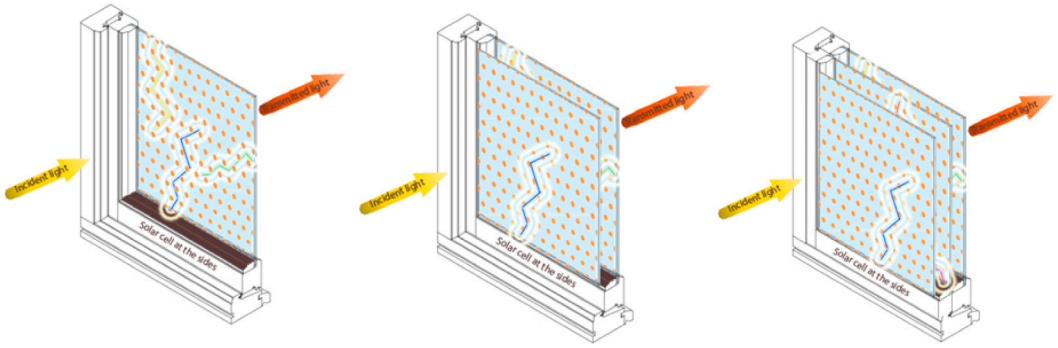

Fig. 1. Single, double (tandem), and triple layered LSC devices. The dot patterns on the windows depict the luminophores. Some of the incident sunlight (yellow arrow) is absorbed and emitted towards the side-mounted PV cells (blue line), and the rest is transmitted (red arrow). (For interpretation of the references to color in this figure legend, the reader is referred to the web version of this article.)

around 2.5% [19], while record power conversion efficiencies (PCE) of 6.8% [20] and 7.1% [21] have been presented. It is speculated that LSCs need a PCE of 10% to be a competitive energy harvesting building element [22,23]. Using the detailed balance approach used by Shockley and Queisser [24], the maximum efficiency of an LSC with an absorption gap between 435–675 nm was calculated by Yang and Lunt to be around 20% for a single junction device with an optimal coupling to a PV device [25]. The practical limits, however, lie around the 10% mark for a device with 100% transparency in the visible [26]. We note that depending on the application, the transparency and device efficiency need to be optimized in combination, i.e., finding a compromise between the lowest acceptable transparency and the highest possible efficiency [27].

The luminophore is the most studied part of the LSC device [5,6]. Options are organic dyes, rare earth ions, and quantum dots (QDs) which are evaluated on their effectiveness in capturing and emitting light. A high-performance luminophore can be characterized by a broad absorption spectrum, a high absorption coefficient, a high luminescent quantum yield (LQY), and a large Stokes' shift [5,28]. The latter denotes the difference between the maximum of the absorption and the maximum of the emission spectrum for the luminophore. This provides a measure for the re-absorption rate: the probability of an emitted photon to be absorbed again by a nearby luminophore and thus a chance for the photon to be lost due to a non-unity LQY [29]. Typically, organic dyes have high LQY but low Stokes' shift [30], while rare-earth ions and QDs can have high Stokes' shift and high LQY [5,28,31]. QDs, or nanoparticles (NPs) in general, show promising results with tunable absorption and emission spectra and consequently high Stokes' shift [32,33], good stability, solubility, and low costs [34]. Therefore, QDs have seen a growing interest in recent years due to their potential for absorbing different wavelengths of incoming light and the potential low-cost production process [28,35]. Studies using Monte Carlo ray tracing mostly focus on efficiency optimization for LSCs. Recently, however, also visual performance has been investigated [35], as it has been shown that the characteristics of transmitted light inside a building has a significant effect on well-being [36], and physical and psychological behavior of its residents [37,38].

Building upon these findings, this paper investigates the differences between various QD materials used in LSCs, further denoted as QDLSCs. In addition, as is the case for conventional PV, the prospects of LSC devices are increased when combining multiple devices by stacking them on top of each other, as illustrated in Fig. 1, to capture a larger part of the incoming solar spectrum. Goetzberger [11] reported already in 1977 on added benefits of a tandem structure because of the higher absorption of sunlight and better compatibility with the side-mounted PV cells, which were crystalline silicon cells at that time.

This paper investigates optimal combinations of eight QD materials for use in single, double, and triple structures through Monte Carlo ray tracing. Results are focused on conversion efficiency and visual performance in order to answer our research question: "What combination of QD luminophores at which specific transmission yields the highest performing single, double and triple LSCs based on conversion efficiency and visual performance?".

The rest of the paper is organized as follows: Section 2 describes the methodology and assumptions. Results for single, double, and triple LSCs are shown and discussed in Section 3. Section 4 presents the conclusions of the research, including recommendations for further research.

2. Methodology

This section describes the ray trace simulations and subsequent determination of performance indicators. The flowchart in Fig. 2 gives an overview and interrelation of the various steps taken.

2.1. Ray trace model

The model used in this report is a Monte Carlo ray trace model based on the PVtrace libraries by Daniel Farrell [39,40]. Ray trace simulations have been widely deployed for LSC system research to assess their efficiencies and losses [4,6,41–45]. In essence, the fate of an incoming photon is followed through the device, including reflection, refraction, absorption, emission, escape, and capture.

The input parameters for a ray trace simulation are the solar spectrum ($S(\lambda)$), the number of photons, the device geometry, the refractive index of the waveguide material PMMA (n_{wg}), the absorption coefficient of PMMA ($c_{PMMA}(\lambda)$), the emission ($E(\lambda)$) and absorption spectrum ($A(\lambda)$) of the luminophore, the luminescent quantum yield (LQY) and the concentration factor of the used luminophore (c_{lm}).

A ray trace model simulates the fate of every single photon individually through the device. It samples using a random number $\xi_{ph} \in [0, 1]$ from a cumulative distribution function based on a probability density integral (Eq. (1)). It is standard practice [46] to use the AM1.5G photon flux in Eq. (1) with a specific interval $[\lambda_{start}, \lambda_{end}]$, e.g., up to near infra-red.

$$\frac{1}{K}\int_{\lambda_{start}}^{\lambda_{end}} \Phi(\lambda)d\lambda = \xi_{ph} \tag{1}$$

in which K is a normalization constant, calculated as $K = \int_0^\infty \Phi(\lambda)d\lambda$, and $\Phi(\lambda)$ is the incoming photon flux.

In this paper, we use 10^6 photons for the simulations, which yields sufficient statistics (low enough noise in the results) for ray-trace simulations [47]. The angle of incidence is perpendicular to the plane of the waveguide. The geometry of the LSC device is set at 0.1 × 0.1 × 0.005 m (L × W × H, with L length, W width, and D thickness). Upon interaction with the LSC device, the reflection or refraction is calculated based on the Fresnel equations for unpolarized light. The

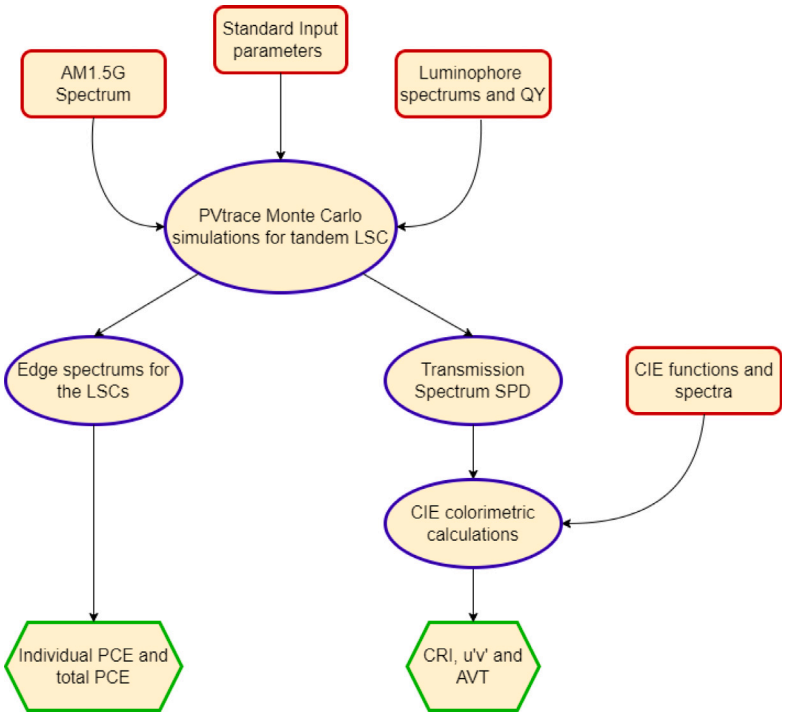

Fig. 2. Flowchart for the ray trace Monte Carlo simulations. Inputs are placed inside the red squares, intermediate results are inside the blue ellipses, and end results are inside the green hexagons. Flow chart based on [35].

calculated reflectance is compared to a random number to equate either reflection or refraction.

If the ray is transmitted into the material, the path length of the ray is determined by comparing to the Lambert–Beer law (Eq. (2)) to a random number $\xi_A \in [0,1]$.

$$\xi_A = 1 - \exp\left(-\epsilon(\lambda) c_{\text{lum}} l\right) \tag{2}$$

Here $\epsilon(\lambda)$ is the absorption coefficient at the wavelength λ, c_{lum} is the concentration of the luminophore, and l is the resulting path length. If the path length falls inside the device geometry of the LSC, the photon is absorbed. Conversely, if the path is longer than the device geometry, the Fresnel equations again determine the chance of reflection or refraction of the ray. To vary the absorption rate and, consequently, the transmittance of the LSC device, the concentration c_{lum} is modified.

If the photon is absorbed, a random number ($\xi_{QY} \in [0,1]$) is picked and compared to the value of the luminophore's LQY to determine if a photon is emitted or not. When a photon is emitted, it is given a direction by specifying a random vector on the unit sphere surrounding the absorption event. Secondly, the wavelength of the emitted photon is determined by sampling from the emission spectrum ($E(\lambda)$) under the condition that the emission wavelength is larger than the absorption wavelength.

$$\frac{1}{K_E}\int_{\lambda_{abs}}^{\infty} E(\lambda)d\lambda = \xi_{QY} \tag{3}$$

in which K_E is a normalization constant given by $K_E = \int_0^{\infty} E(\lambda)d\lambda$. If the emission occurs outside the escape cone, the photon will internally reflect towards the sides, where it can be captured for electricity generation.

In a tandem configuration, rays exiting the first LSC, either transmitted or inside the escape cone, will undergo the same procedure again for a second and a third LSC in a triple configuration. These LSCs are modeled to be situated directly underneath each other with an air gap ($n = 1.0$) of 0.05 m and identical geometry. The PVtrace [40] algorithm allows for visualization of the complete device, shown for a triple tandem LSC in Fig. 3 for a test setting with CdSe/CdS Cu doped as the luminophore. The incident rays, the rays emitted towards the sides of the LSCs, and the transmitted rays are collected in order to calculate key performance indicators, such as total device conversion efficiency.

2.2. Key performance indicators

Two factors play a key role for an LSC to function effectively as a window: the generated amount of electricity and the transmitted light. The former is assessed with LSC device efficiency, and the latter with visual performance calculations.

2.2.1. LSC efficiency

There is a multitude of ways to assess the efficiency of an LSC. The first defines the ratio between the number of photons collected from the four waveguide faces at the sides, and the total incident photons, which is denoted as External Quantum Efficiency (EQE), Eq. (4) [26,48]. The Internal Quantum Efficiency (IQE) is similar to the EQE but excludes reflected photons, Eq. (5) [26]. In this paper, we assume photons incident perpendicular to the top surface, which leads to 4% reflection loss based on Fresnel equations and the refractive index of PMMA (1.5). We note that the equations have a slightly different meaning compared to conventional PV, as photon numbers are used here instead of collected electrons.

$$EQE = \frac{\Phi_{out}}{\Phi_{in}} \tag{4}$$

$$IQE = \frac{\Phi_{out}}{\Phi_{abs}} = \frac{EQE}{1-R} \tag{5}$$

with Φ_{out} is the flux of photons collected at the sides (number/s), Φ_{in} flux of incoming photons (number/s), Φ_{abs} flux of absorbed and transmitted photons (number/s), and R the reflection coefficient calculated with Fresnel equations.

As EQE and IQE use the ratio of photons but disregard the energy of the photons, another measure is also used, namely the Optical Efficiency (OE), see Eq. (6). It takes the output power from the edges of all photons over the input power from the top of the LSC for the

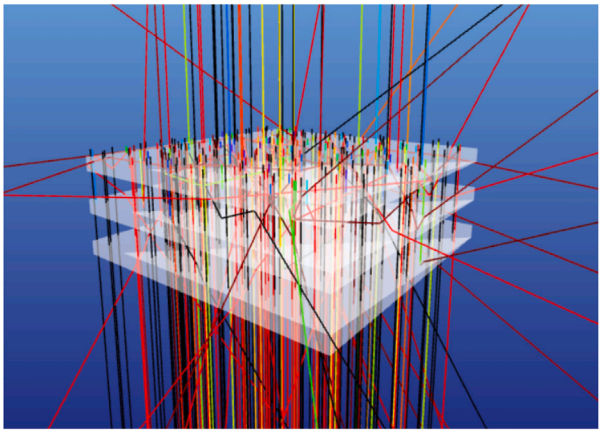

Fig. 3. Visual representation of PVtrace generating 300 rays emitted from an AM1.5G spectrum incident on three LSC plates, each with CdSe/CdS Cu doped as a luminophore. The figure shows the light being emitted to the sides and shifted to red wavelengths (the colors correspond to the wavelengths) according to the absorption and emission spectrum of CdSe/CdS Cu doped. (For interpretation of the references to color in this figure legend, the reader is referred to the web version of this article.)

wavelength range specified in the simulation [30]. Note that both efficiency measurements are dependent on the transmission.

$$OE = \frac{P_{out}}{P_{in}} = \frac{\int S_{out}(\lambda)d\lambda}{\int S_{in}(\lambda)d\lambda} \tag{6}$$

The final indicator is the Power Conversion Efficiency (PCE) [30] given by Eq. (7). Here, J_{SC} is the short circuit current density of the PV cell(s) attached to the sides of the waveguide in A m^{-2}, V_{OC} is the open circuit voltage in Volt, I_{SC} is the short-circuit current in Ampere, FF is the fill factor and P_{in} is the power density of the incident solar radiation (under standard test conditions this is usually taken at 1000 W m^{-2} for AM1.5G solar radiation) [30].

$$PCE = \frac{V_{OC}\ J_{SC}\ FF}{P_{in}} = \frac{V_{OC}\ I_{SC}\ FF}{A_{top}P_{in}} \tag{7}$$

Note that A_{top} is the area of the LSC onto which the photons are impinging, not the area of the PV cells (A_{PV}). A geometrical concentration (G_X) ratio is defined as

$$G_X = \frac{A_{top}}{A_{PV}} \geq \frac{L\ W}{2(L+W)\ H} \tag{8}$$

in which it is assumed that all four sides are fully covered with PV cells. If not, the greater-than symbol applies. In this paper, $G_X = L/4H = 5$ (for square geometry $L = W$).

The data for calculating the EQE, IQE, and OE is taken from photon flux values resulting from the simulations. For PCE, additional data is needed for the attached PV cell. Data for the attached PV cell has been taken from Yoshikawa et al. (2017) [49], who use a silicon heterojunction cell with interdigitated back contacts which is ideal for coupling with an LSC device (no shading losses from contacts). This cell has a record STC efficiency of 26.3%, $J_{SC} = 42.3$ mA/cm^2, $V_{OC} = 0.744$ V, and $FF = 0.838$. EQE is shown in Appendix A.1

To calculate the PCE, the incoming photon flux per wavelength is multiplied by the efficiency of the solar cell at that wavelength [49] and elementary charge q. This gives the generated number of electrons per wavelength, which can be integrated to determine total short-circuit current (J_{SC}), as follows:

$$J_{SC} = q\int_{\lambda_1}^{\lambda_2} \Phi_{in}(\lambda)EQE(\lambda)d\lambda \tag{9}$$

The calculation of the short-circuit current density in this manner is common practice in LSC simulations [35,50]. In this paper, we model one second of incoming AM1.5G solar radiation. As the photon flux is $4.3 * 10^{21}$ s^{-1} m^{-2}, a correction factor of $4.3 * 10^{13}$ is needed as we simulated 10^6 photons on a 0.01 m^2 surface.

With the short-circuit known, the open-circuit voltage (V_{OC}) can be calculated as follows, assuming an ideal diode curve, i.e., series and shunt resistances and non-ideal diode quality factor can be ignored:

$$V_{OC} = \frac{k_B T}{q}\left(\ln\frac{J_{SC}}{J_s} + 1\right) \tag{10}$$

by using the diode saturation current density (J_s) as provided by Yoshikawa et al. [49], the Boltzmann constant (k_B) and the temperature (T), which is taken as 300 K.

The fill factor can be calculated assuming that series and shunt resistance values, and non-ideal diode quality factor can be ignored, by using Green's relation [51] between fill factor and normalized V_{OC}, defined as $v_{OC} = qV_{OC}/k_BT$:

$$FF = \frac{v_{OC} - \ln\left(v_{OC} + 0.72\right)}{v_{OC} + 1} \tag{11}$$

Power generated by the solar cells P_{mpp} then is

$$P_{mpp} = FFV_{OC}I_{SC} = V_{mpp}I_{mpp} \tag{12}$$

Taking the derivative of the power versus voltage curve, the voltage at the maximum power point V_{mpp} is found to be:

$$V_{mpp} = V_{OC} - \frac{k_B T}{q}\ln\left(\frac{qV_{mpp}}{k_B T} + 1\right) \tag{13}$$

This implicit equation for V_{mpp} can be solved iteratively. With FF known, I_{mpp} can be calculated.

2.2.2. Visual performance

In order for LSCs to substitute windows in the building envelope, the transmitted light needs to be analyzed. It has been shown that an LSC will alter the spectral distribution of the incoming solar radiation resulting in different color qualities [52]. The science of assessing the visual performance of incoming light is called colorimetry and is frequently used in glass and glazing applications [53].

Colorimetrics rely on the widely used Color Rendering Index (CRI), which quantitatively denotes the accuracy of the colors of an object with respect to an 'ideal' illumination source. The value of CRI ranges between 0 and 100, with 100 being a perfect representation of the colors of the object. A CRI of at least 70 is considered to be of good quality [9] and a CRI above 85 is of superior quality [26,54]. Since the perception of colors is always based on the viewer, colors are evaluated with respect to a reference source. This source is denoted as D65, which represents average midday light in Western Europe as defined by the Commission Internationale de l'Eclairage (CIE), the general authority on colorimetrics [55].

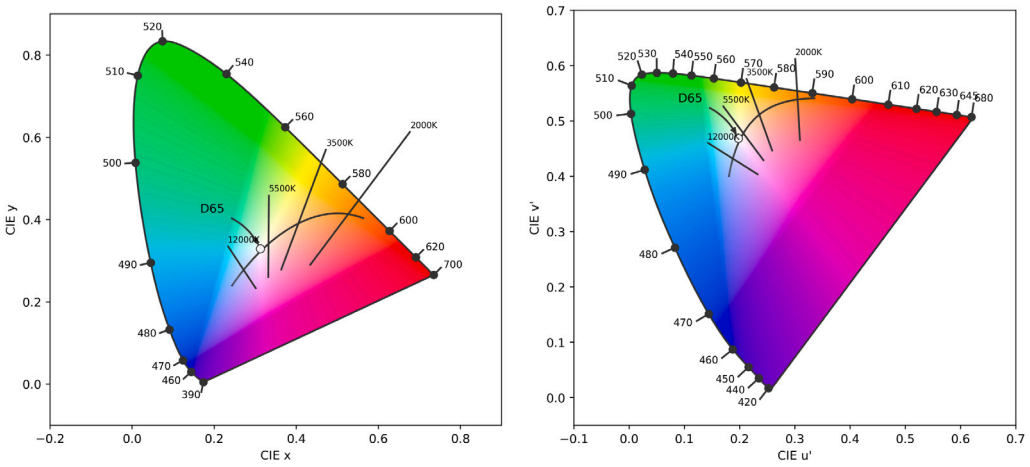

Fig. 4. Two chromaticity diagrams showing the color and correlated color temperature of D65. (a) shows the xy-chromaticity and (b) the $u'v'$-chromaticity. The extended lines represent the same correlated color temperature and are called isotherms. (For interpretation of the references to color in this figure legend, the reader is referred to the web version of this article.)
Source: Image from [35].

In order to calculate the CRI, first, the tristimulus values (X, Y, Z) are calculated from the transmitted light and the color-matching functions representing the spectral response of the human eye. These tristimulus values are subsequently used to visualize the color in a 2D xy-chromaticity diagram and the more representative $u'v'$-chromaticity diagram [56], see Fig. 4, which we will use in this paper.

From the chromaticity diagrams the Correlated Color Temperature (CCT) can be determined. This is the temperature of the color as emitted by a black-body radiator [35]. For example, the AM1.5G spectrum can be approximated when taking the sun as a black body radiator with a temperature around 6000 K. Conceptually, it can be thought of as the 'warmth' of the color with, counter-intuitively, higher CCT values producing 'colder' colors.

The CIE replaced the well-known R, G, B values (Red, Green, Blue) in 1931 to become more practical [35,55]. The tristimulus values can be calculated if the Spectral Power Density (SPD) is known, i.e., the radiation power at each wavelength. Furthermore, the tristimulus values depend on the color matching functions $\bar{x}$, $\bar{y}$ and $\bar{z}$, which indicate how the human eye responds to certain wavelengths and a constant K = 683 lm/W, as follows:

$$X = K \int_{vis} P_T(\lambda)\bar{x}(\lambda)d\lambda \tag{14}$$

$$Y = K \int_{vis} P_T(\lambda)\bar{y}(\lambda)d\lambda \tag{15}$$

$$Z = K \int_{vis} P_T(\lambda)\bar{z}(\lambda)d\lambda \tag{16}$$

Here, $P_T(\lambda)$ represents the radiant power of the transmitted light of the LSC devices, and the visible spectrum ranges from 380 to 700 nm.

To calculate the transmitted light's chromaticity values, the tristimulus values X, Y, and Z are divided by their sum to get the relative values x and y. Since the total of the relative sum is equal to 1, only two values are necessary to indicate the color (Eqs. (17) and (18)).

$$x = \frac{X}{X+Y+Z} \tag{17}$$

$$y = \frac{Y}{X+Y+Z} \tag{18}$$

$$z = 1 - x - y \tag{19}$$

The x and y values are used to calculate the CIE 1964 chromaticity diagram [55], see Fig. 4(a). However, a disadvantage of this method is that not all colors are represented by the same area [57]. Therefore, the CIE has designed the CIE 1976 CIE L* u* v* color space, which can be easily computed from the chromaticity values x and y and uses u' and v' [56] see Fig. 4(b) [35]. The equations for calculating u' and v' are:

$$u' = \frac{4x}{-2x + 12y + 3} \tag{20}$$

$$v' = \frac{9y}{-2x + 12y + 3} \tag{21}$$

From the chromaticity diagram, CCT can be determined by plotting a color on a $u'v'$ diagram and finding the corresponding color a black-body radiator would emit. Since these black-body radiators always emit all wavelengths, multiple points will have the same CCT in a chromaticity diagram. The points having the same CCT are depicted by the lines in Fig. 4 and are called isotherms. The full path of the line is denoted as the Planckian locus or black body locus.

The color rendering index indicates the potential of the transmitted light to correctly display the color of an object [9]. A color appearance model is used to evaluate a color's perceptual attributes. There is a multitude of color appearance models ranging in complexity and consideration of environmental factors. The oldest and default option is the UVW method [53]. Besides the UVW, the CIELUV color appearance model has been proposed. This slightly alters the UVW lightness scale $W*$ and the coordinate $v*$ [58], the CIELUV method is optimized for self-luminous color displays [35].

The main difference between a color appearance model and a chromaticity diagram is the lightness factor $W*$, which depicts the relative brightness of a color. It can be thought of as representing the color on a grayscale. The equations for UVW uniform color space are:

$$W* = 25Y^{\frac{1}{3}} - 17 \tag{22}$$

$$u* = 13W*(u' - u'_n) \tag{23}$$

$$v* = 13W*(v' - v'_n) \tag{24}$$

Here Y is the relative tristimulus value (Eq. (14)), which is normalized to 100, and u' and v' depict the chromaticity coordinates of the measured light and u'_n and v'_n are the chromaticity coordinates of the relative white color.

Since colors are always relative, the CRI is determined by comparing the transmitted light to fourteen Munsell test colors determined by the CIE [55] that span the entire visible region. When compared with a color, there will be a certain distance in lightness $W*$, and the $u*$ and

Table 1
Properties of quantum dots.

QD material	Emission (nm)	Luminescent quantum yield (%)	Source
CdSe/CdS giant shell	640	50	[63]
ZnSe/ZnS Mn^{2+} doped	590	50	[67]
CdSe Cu doped	705	70	[68]
PbS/CdS	890	50	[64]
CuInSeS/ZnS	960	40	[65]
AgInS/ZnS	900	30	[66]
Si	830	45	[69]
C	550	40	[70]

$v*$ values. This difference is taken as the Euclidean distance between two points (Eq. (25)) and shows the color shift.

$$\Delta E = \sqrt{(\Delta W*)^2 + (\Delta u*)^2 + (\Delta v*)^2} \tag{25}$$

The color difference ΔE is calculated for every color, and subsequently, the specific CRI ($R_i = 100 - \Delta E_i$) can be obtained. The mean value of CRI then shows the ability of the transmitted light to show the actual color of an object and should be as high as possible. Recent LSC research uses the method by Yang and Lunt [59] based on these calculations, which is also adopted in this paper.

$$CRI = \frac{1}{14}\sum_{i=1}^{14} R_i \tag{26}$$

2.2.3. Light Utilization Efficiency

Since the transmitted light serves a clear purpose in LSC devices, a new metric has been proposed by Traverse et al. [9], which combines the PCE and the Average Visible Transmission (AVT): the Light Utilization Efficiency (LUE).

The AVT is defined as the ratio of the incident and transmitted light, weighted by the visible spectrum of the human eye [26,30]:

$$AVT = \frac{\int T(\lambda)P(\lambda)S(\lambda)d(\lambda)}{\int P(\lambda)S(\lambda)d(\lambda)} \tag{27}$$

in which T is the transmission as a function of λ, P is the spectral sensitivity of the human eye also called the photopic response [60], and S is the solar photon flux (AM1.5G). We note that $\int S(\lambda)d(\lambda) = 1000$ W/m^2, and $\int P(\lambda)S(\lambda)d(\lambda) = 180$ W/m^2, using a wavelength range of 280–4000 nm for the full spectrum and 380–700 nm for the photopic response. Some typical AVT values are 92% for quartz glass and 80% for double-paned insulated glass [61]. Generally, glass with a value above 60% looks clear, and below 50% will look tinted [62].

Light Utilization Efficiency is defined as:

$$LUE = PCE \times AVT \tag{28}$$

LUE reflects that high PCE will compromise high AVT and vice versa, and LUE as a function of AVT typically show a maximum around AVT = 50% [9].

2.3. QD data

In this study, the same quantum dots are used as in Moraitis et al. (2019) [35], which were found to be suitable for large-scale production of QD-based LSCs. The emission and absorption spectra of these QDs have been obtained in previous studies by spectroscopic measurements. In total, eight different QDs are shown in Fig. 5. Emission peak and quantum yield are shown in Table 1. The figure shows that the selected QDs have a large Stokes shift, reducing re-absorption losses, while some overlap remains between the absorption and emission spectrum in all cases. These large Stokes shifts can be obtained by semiconductor core–shell structures [63–66], doping [67,68], and single material QDs (Si, C) [69,70].

Table 2
Configurations for tandem LSCs based on the requirements for absorption/emission overlap and quantum yield ($QY > 50\%$) for the top LSC waveguide. Configurations are labeled Di, with i a number.

Configuration	Top luminophore	Bottom luminophore
D1	CdSe/CdS giant shell	PbS/CdS
D2	"	CuInSeS/ZnS
D3	"	Si
D4	ZnSe/ZnS Mn^{2+} doped	CdSe/CdS Cu doped
D5	"	PbS/CdS
D6	"	CuInSeS/ZnS
D7	"	C
D8	"	AgInS/ZnS
D9	CdSe/CdS Cu doped	PbS/CdS
D10	"	CuInSeS/ZnS
D11	"	Si
D12	PbS/CdS	PbS/CdS
D13	"	CuInSeS/ZnS
D14	"	Si

2.4. Criteria for double/triple LSCs

To limit the number of simulations, some criteria are used. In principle, for a double configuration, $8^2 = 64$ would be possible, and for a triple $8^3 = 512$. In a double or triple LSC device, the top LSC should contain luminophores with a large LQY and an absorption spectrum near UV-wavelengths [11,72]. For the top waveguide, all luminophores with a LQY of 50% or more are thus selected in this paper. For double LSCs, the bottom waveguide could contain any of the other luminophores as long as the absorption spectrum is in the range of the emission spectrum of the luminophore of the top LSC. This allows for absorption by the bottom waveguide of transmitted and emitted light from the top one. The resulting 15 LSC configurations fulfilling these criteria are listed in Table 2.

For triple LSCs, the middle and bottom waveguide can contain any of the other luminophores, as long as some overlap with the emission spectrum of the waveguide above it is present, but no LQY limitations are set. An example of a possible triple tandem LSC would be CdSe/CdS Cu doped//CuInSeS/ZnS//PbS/CdS. This has been selected since the LQY of CdSe/CdS Cu doped is 70% and there is at least some overlap in the absorption and emission spectra as visible in Fig. 5c–e. This enables the escaped photons from the top LSC to be captured by the middle and/or bottom waveguides. A list of all 45 combinations for triple LSC configurations is shown in the Appendix A.2, Table A.1.

2.5. Setting AVT

Since the absorption and emission spectra are based on relative units the single, double and triple LSC configurations have been tested based on the percentage transmitted light (AVT) compared to incident light. It should be noted that the AVT strongly depends on the photopic response curve and the specific QD absorption spectra. Fig. 6 illustrates that absorption spectra of the used QDs overlap differently with the photopic response curve $P(\lambda)$. For example, the absorption spectrum of the CdSe/CdS giant shell is rather flat in the wavelength range of the photopic response, while the Si absorption spectrum hardly overlaps. This means that the actual concentration of Si QDs will be much higher than that of the CdSe/CdS giant shell in order to reach the same AVT. This will not lead to much higher PCE, as the number of photons of the incident AM1.5G spectrum is low compared to the number in the visible range.

For single LSC configurations, concentrations for each QD have been varied to determine the relationship between the absorption coefficient and AVT. In this way, by adjusting concentrations, AVT values of 65%, 75%, and 85% for each luminophore are found.

For a double structure, luminophore concentrations for each waveguide are varied such that AVT values of 65%, 75%, and 85% are set for

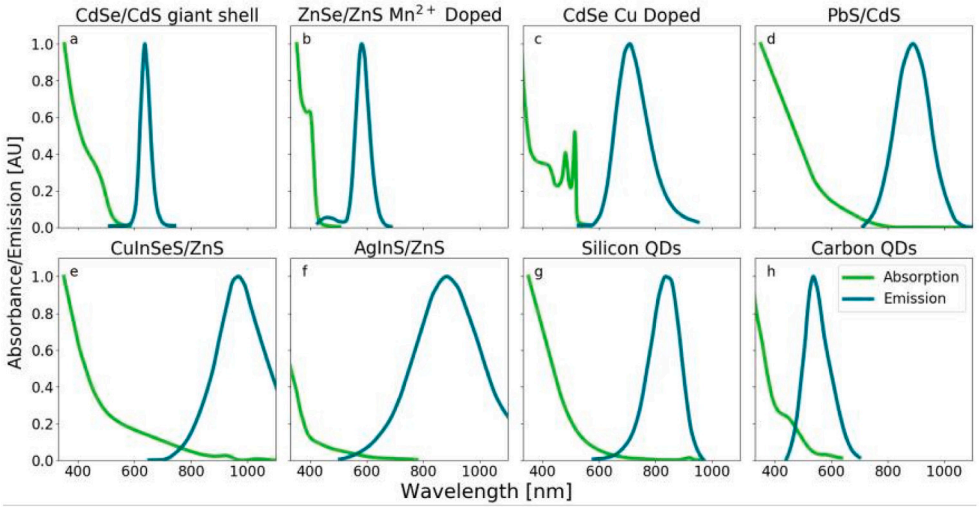

Fig. 5. Absorption and emission spectra for the used QDs. (a) Semiconductor CdSe/CdS quantum dots with core–shell structure [63]. (b) ZnSe/ZnS with core–shell structure doped with Mn^{2+} [67]. (c) Semiconductor CdSe/CdS Cu doped quantum dots with core–shell structure [68]. (d) Core–shell PbS/CdS quantum dots [64]. (e) Non-toxic semiconductor CuInSeS/ZnS quantum dots with core–shell structure [65]. (f) AgInS/ZnS nanocrystals [66]. (g) Silicon quantum dots [71]. (h) Colloidal carbon dots [70].
Source: Graph from Moraitis et al. (2019) [35].

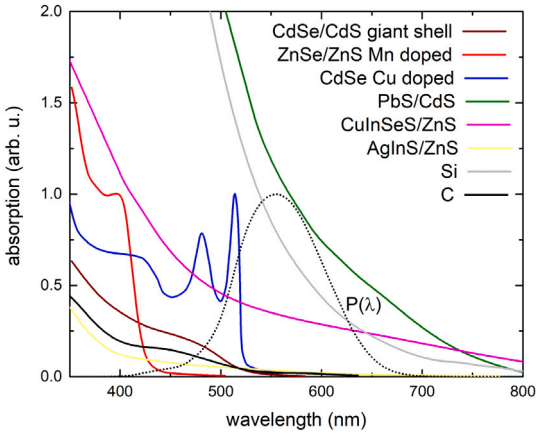

Fig. 6. Absorption spectra for the used QDs in comparison to the photopic response $P(\lambda)$ (dotted line).

individual waveguides. Depending on the QD combinations, the AVT of the double structure will be lower than the single structures. Also for the triple configuration, these values for AVT have been used. This leads to LSC configurations spanning a range in AVT between 25% and 85%.

3. Results

3.1. Single LSCs

Fig. 7 depicts PCE, CRI, CCT, and LUE as a function of LQY for the eight QDs used, for three different values of AVT. It is clear from Fig. 7a that QDLSCs with QDs with larger LQY lead to larger values of PCE, as indicated by the linear fits. Also, the larger the AVT, the lower the PCE. Differences in results for different QDs are due to differences in absorption range. For example, the three QDs with LQY of 50%, namely CdSe/CdS giant shell, PbS/CdS, and ZnSe/ZnS Mn doped do not differ much in PCE (1.0–1.3%, for AVT = 65%), while the two QDs with QY of 40%, namely Carbon and CuInSeS/ZnS have larger differences (0.33–1.06%). The best PCE is 2.02% for an LSC with CdSe/Se Cu doped as luminophore, at AVT = 65%, CRI 45.9, and CCT of 2534 K.

The analysis shows that both CRI and CCT decrease with decreasing AVT, but increase with lowering LQY. At higher LQY more red-shifted photons are emitted, leading to spectral changes that adversely affect CRI. The results show that single QDLSCs should have AVT > 75% to have acceptable CRI and CCT for indoor comfort. LUE increases with LQY, as more emitted photons will reach the PV cells, but it decreases with increasing AVT, as fewer photons are absorbed. The CIE $u'v'$ diagrams are shown in Fig. 8a and b. Larger AVT values in general lead to higher u' and v' values such that the transmitted light appears yellow/orange (between 570–580 nm).

3.2. Double LSCs

Fig. 9 depicts PCE for all configurations listed in Table 2. The graphs distinguish PCE for the four different top luminophores. The best efficiency of 2.4% is found for a configuration with CdSe/CdS Cu doped in the top waveguide and PbS/CdS or CuInSeS/ZnS in the bottom waveguide. AVT values are 45 and 44%, for PbS/CdS and CuInSeS/ZnS, respectively. CRI and CCT are 38 and 41, and 2293 and 2400 K, respectively. From the inside, this LSC appears yellow/brown (582 nm, see Fig. 8c).

Fig. 9 also shows that the contribution to the PCE of the top waveguide is larger than the bottom one. In fact, the bottom waveguide adds (22 ± 10)% relative to total PCE, depending on actual QDs used. This can be explained by looking at the spectral overlap of the emission spectrum of the luminophore in the top waveguide (CdSe/CdS Cu doped) and the absorption spectrum of the bottom waveguide luminophore (PbS/CdS). Defining spectral overlap as $\int A_{top}(\lambda)E_{bottom}(\lambda)$ using data in Fig. 10 yields a value of 46.6 in arbitrary units. Only the higher energy emitted photons from the top waveguide will be absorbed by the bottom waveguide luminophore. A QD with a larger absorption cut-off wavelength would lead to higher PCE.

3.3. Triple LSCs

The highest efficiency of 2.7% is found for a configuration with CdSe/CdS Cu doped in the top waveguide, PbS/CdS (or CuInSeS/ZnS) in the middle waveguide, and CuInSeS/ZnS in the bottom waveguide, with AVT = 30.3% (29.4%), CRI = 33.5 (36.6) and CCT = 2243 K (2317 K). From the inside, this LSC appears yellow/brown (585 nm, see Fig. 8d).

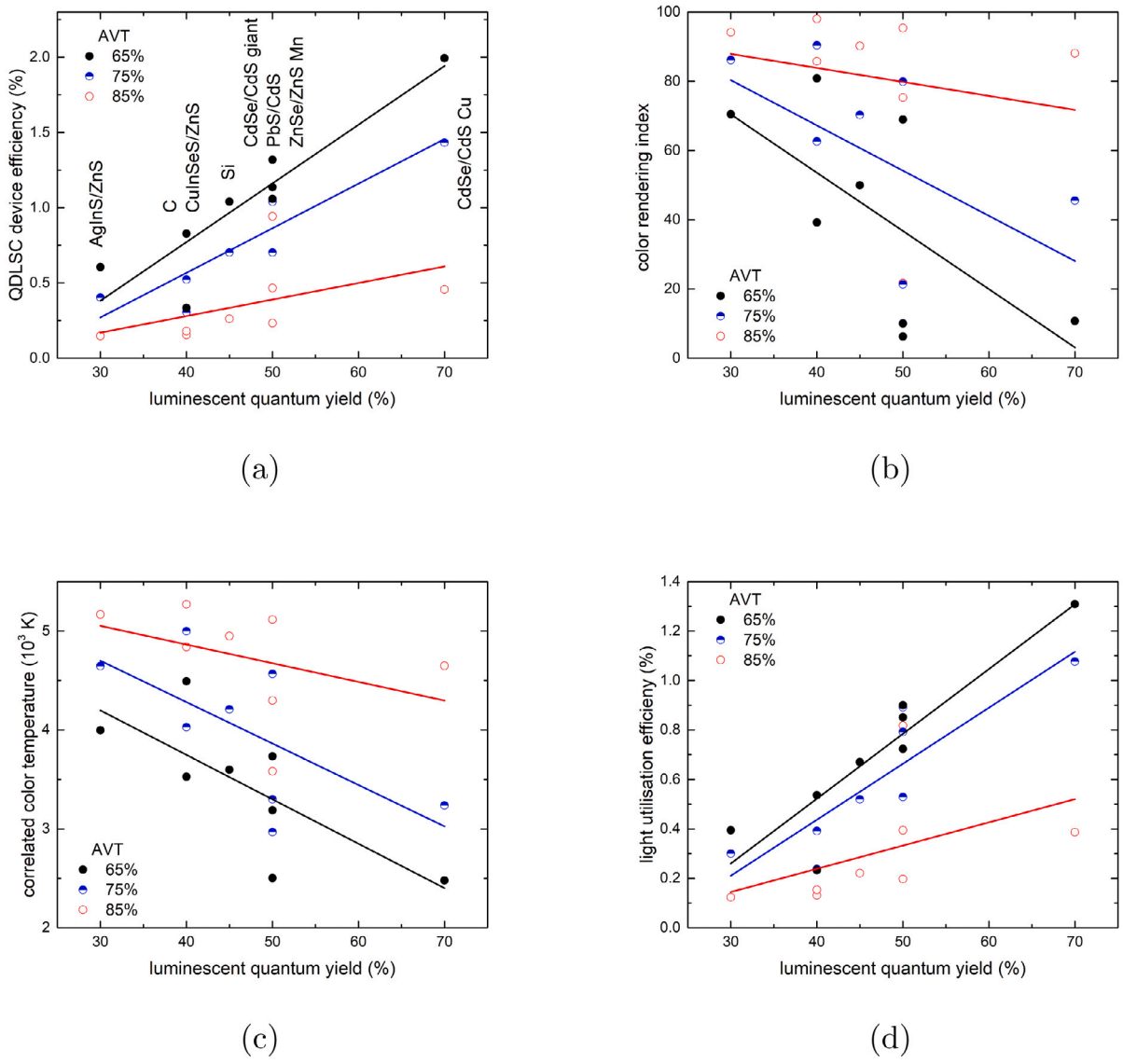

Fig. 7. QDLSC device efficiency (PCE) (a), color rendering index (CRI) (b), correlated color (CCT) (c), and light utilization efficiency (LUE) (d) for single QDLSC waveguides with the used QDs, as a function of their quantum yield for three different values of average visible transmittance. Lines are guides to the eye. (For interpretation of the references to color in this figure legend, the reader is referred to the web version of this article.)

As in the case of double LSC configurations, the top waveguide contributes most to the total PCE, as shown in Fig. 11. For the triple configuration, the middle and bottom contribute 17(±8)% and 13(±5)% to total PCE, respectively. This can also be explained by investigating the spectral overlap in absorption and emission spectra. Defining spectral overlap as $\int Abs_{top} Em_{middle}$ using data in Fig. 12a yields a value of 42.3 in arbitrary units, which is slightly lower than the value of the double LSC for which CuInSeS/ZnS also was a good candidate. The spectral overlap between middle and bottom LSC, defined as $\int Abs_{middle} Em_{bottom}$ yields 5.5 in arbitrary units. The bottom LSC contributes little (10% relative) to the final device efficiency.

An AVT of 85% for identical luminophores in every waveguide in a triple configuration would give an AVT of 61.4% for the complete configuration. For an AVT of 75% and 65%, this yields 42.2% and 27.5%, respectively, as visualized in Fig. 11. We note that as we combine different luminophores, the reported AVT values are always larger than the indicated values.

3.4. PCE and LUE

Fig. 13 provides a summary of all simulation results, combining single, double, and triple configurations in one graph for PCE and LUE. It is clear that PCE increases with decreasing AVT and depending on the used luminophores, single LSCs can outperform double and even triple configurations. Also, double configurations can outperform triple ones. The LUE versus AVT graph shows an optimum around AVT = 50%, in correspondence with Traverse et al. [9]. We note that the PCE of single LSCs are 1%–2% lower than the PCE of the top in double and triple configurations, which is due to reflection and/or absorption from middle and bottom waveguides.

4. Discussion

In this paper, the results for single LSCs are very similar, but not identical to the earlier work of Moraitis et al. [35], who used the same QDs. This is most likely due to a version change in the used PVtrace algorithm in combination with the complexity of the input parameters.

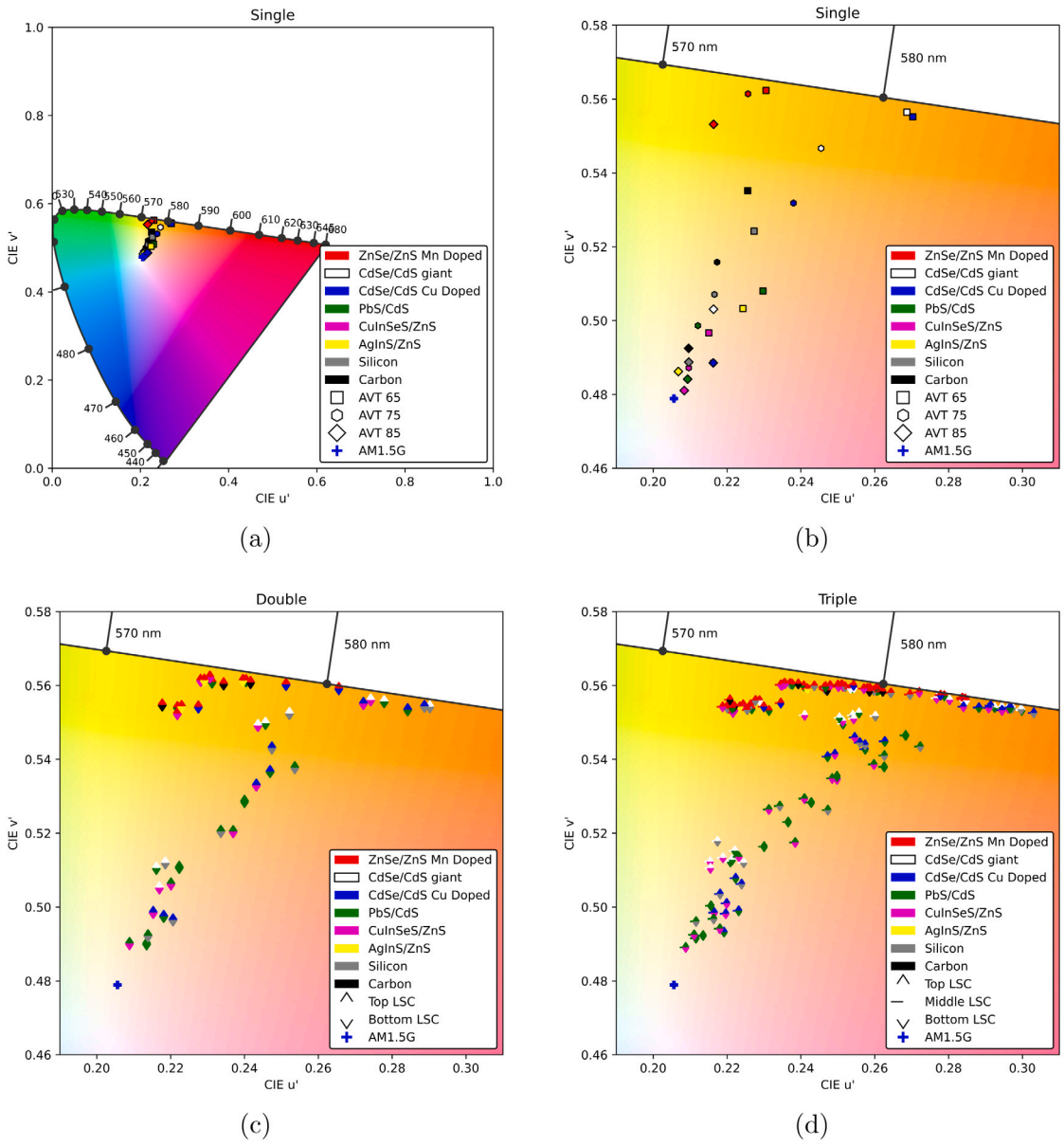

Fig. 8. CIE $u'v'$ diagrams for single (a) and (b) (zoomed in), double (c), and triple (d) configurations. Also, the AM1.5G point is indicated. (For interpretation of the references to color in this figure legend, the reader is referred to the web version of this article.)

Discrepancies with experimental results, if they were available, could arise from data gathered for the luminophores. While these have been taken from acknowledged scientific papers, any nuance in those papers has been disregarded for the sake of the simulation. Also, reported quantum yields are often reported with a variation of a few percent e.g. PbS/CdS has a LQY variation of 10% [64]. An uncertainty analysis should be performed to study the effect of those variations. This was beyond the scope of this paper.

Statistical uncertainty could be associated with the fact that 10^6 simulated photons is not sufficient for definite conclusions, while we note that other ray trace simulations use the same number [47]. Testing with a higher amount of photons should be done in a further study to improve accuracy.

Another important aspect of the report is the choice of input parameters that have been tailored to the minimum known absorption for the quantum dots at 352 nm. This does exclude a significant portion of the light up until 280 nm with high-energy photons. We have chosen not to extrapolate absorption data to lower wavelengths, since it may lead to higher inaccuracies.

The solar cell taken from Yoshikawa et al. [49] determines the power conversion efficiency and could potentially be improved upon, but this already is a very efficient solar cell with interdigitated back-contacts for extra efficiency gains and is ideal for coupling with LSCs. However, zero series resistance and infinite shunt resistance and ideal diode behavior that we assume will slightly overestimate PCE.

In the simulations, we assume cells to be at every side of the waveguides, so having 4, 8, and 12 identical rectangular (silicon) cells for single, double, and triple configuration, respectively. In practice, it may be technologically less complex to use only 4 cells, of different sizes (or even materials) to optimize photon harvesting. This may affect PCE values.

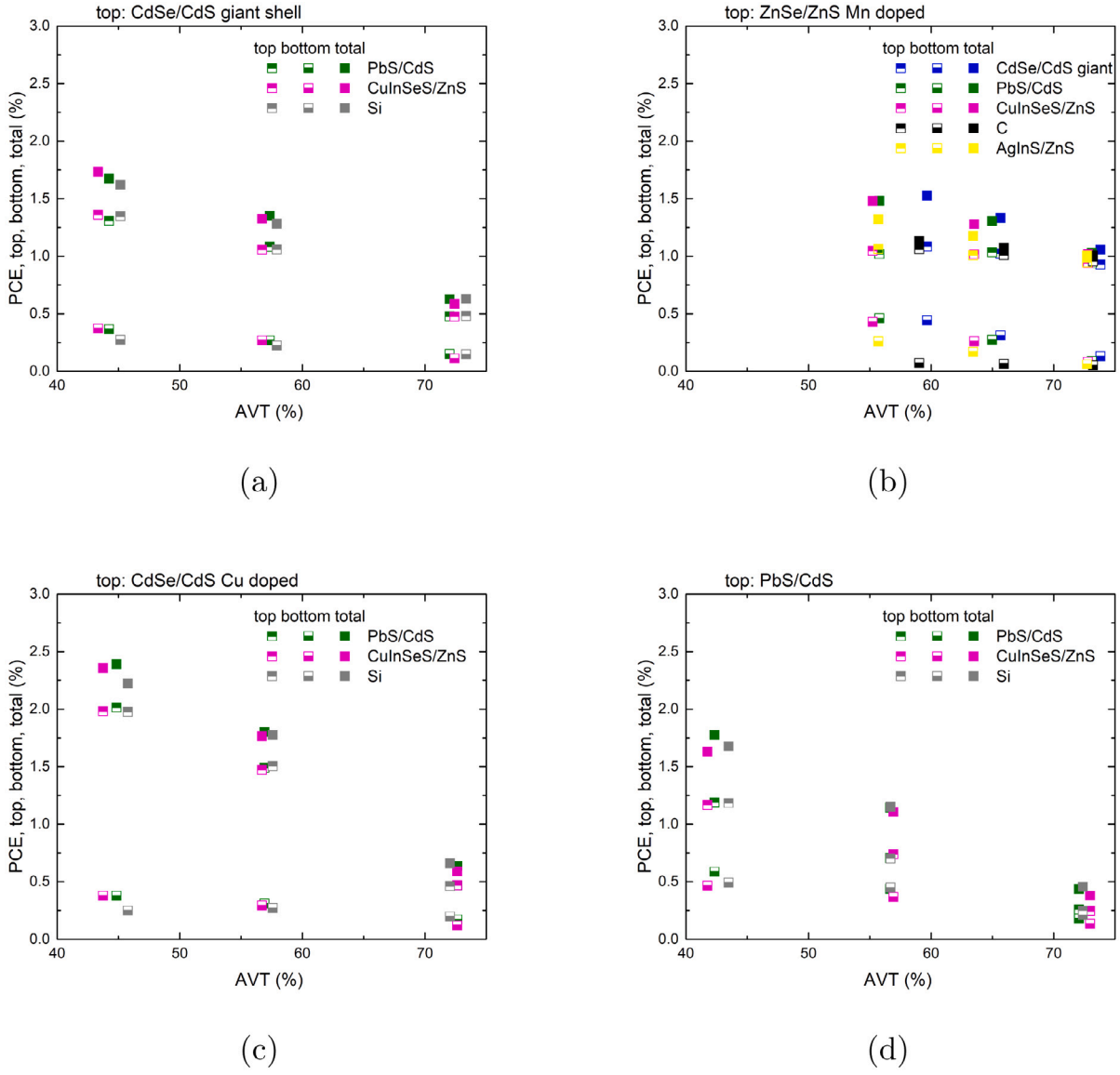

Fig. 9. PCE of double configurations with as (a) CdSe/CdS giant shell, (b) ZnSe/ZnS Mn^{2+} doped, (c) CdSe Cu doped, and (d) PbS/CdS as luminophore in the top waveguide, for all configurations given in Table 2.

4.1. Future research

In our work, we have used three values of AVT for each waveguide in single, double, and triple configurations. Future work will encompass sampling random configurations with random AVT values, thus following a combinatorial approach. In this way, mapping relationships between various variables would be possible, which would aid in quick LSC designs. However, due to the computational intensive ray trace method, this will take time, and a faster method may need to be developed.

The properties of the used QDs date back a few years. Updating, especially *LQY*, will need to be done. Also, other QD materials in terms of absorption and emission spectra and their matching in double and/or triple structures will be searched for in recent literature. The PCE values presented in this paper should be regarded as conservative.

The light utilization efficiency metric was designed by Traverse et al. [9] to indicate the quality of window applications which double as an electricity generating device, and it can be used for all transparent PV devices. Our results corroborate that high LUE often corresponds to a well-performing LSC, but a lot of variation is observed, depending on the materials used. The LUE is based on the photopic response of the human eye. This spectrum stretches from 400 nm to 700 nm. Our results show that high LUE values could be obtained with the purple and blue wavelengths being transmitted, which does not correspond to a high color quality (low CRI). Hence, the LUE is a useful measurement tool if the transmitted spectrum is not heavily skewed nor lacks specific wavelengths. It does provide a valuable measurement tool when the overall average transmission has an even distribution. An option would be to replace the photopic response with the tristimulus values. This would encompass the different colors and punish heavily skewed transmission spectra thus corresponding better to CRI values. A modified LUE or a new metric including the spectral overlap of absorption and emission spectra of the used luminophores would ideally allow for fast prediction of potential PCE. The quality factor as defined by Klimov et al. [73] could be a good starting point.

5. Conclusion

This paper has investigated the electrical performance and colorimetric properties of single, double, and triple configuration LSCs,

Table A.1
Configurations for triple LSCs based on the requirements for absorption/emission overlap and quantum yield ($LQY > 50\%$) for the top LSC waveguide. Configurations are labeled Ti, with i a number.

Configuration	Top luminophore	Middle luminophore	Bottom luminophore
T1	CdSe/CdS giant shell	PbS/CdS	PbS/CdS
T2	"	"	CuInSeS/ZnS
T3	"	"	Si
T4	"	CuInSeS/ZnS	PbS/CdS
T5	"	"	CuInSeS/ZnS
T6	"	"	Si
T7	"	Si	PbS/CdS
T8	"	"	CuInSeS/ZnS
T9	ZnSe/ZnS Mn^{2+} doped	CdSe/CdS Cu doped	PbS/CdS
T10	"	"	CuInSeS/ZnS
T11	"	"	Si
T12	"	PbS/CdS	PbS/CdS
T13	"	"	CuInSeS/ZnS
T14	"	"	Si
T15	"	CuInSeS/ZnS	PbS/CdS
T15	"	"	CuInSeS/ZnS
T16	"	"	Si
T17	"	AgInS/ZnS	CdSe/CdS giant shell
T18	"	"	CdSe/CdS Cu doped
T19	"	"	PbS/CdS
T20	"	"	CuInSeS/ZnS
T21	"	"	Si
T22	"	"	AgInS/ZnS
T23	"	"	C
T24	"	C	CdSe/CdS giant shell
T25	"	"	CdSe Cu doped
T26	"	"	PbS/CdS
T27	"	"	CuInSeS/ZnS
T28	"	"	Si
T29	"	"	C
T30	CdSe/CdS Cu doped	PbS/CdS	PbS/CdS
T31	"	"	CuInSeS/ZnS
T32	"	"	Si
T33	"	CuInSeS/ZnS	PbS/CdS
T34	"	"	CuInSeS/ZnS
T35	"	"	Si
T36	"	Si	PbS/CdS
T37	"	"	CuInSeS/ZnS
T38	PbS/CdS	PbS/CdS	PbS/CdS
T39	"	"	CuInSeS/ZnS
T40	"	"	Si
T41	"	CuInSeS/ZnS	PbS/CdS
T42	"	"	CuInSeS/ZnS
T43	"	"	Si
T44	"	Si	PbS/CdS
T45	"	"	CuInSeS/ZnS

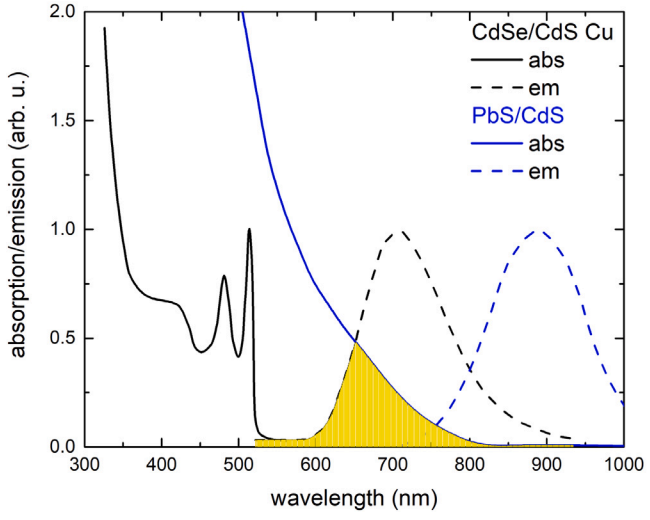

Fig. 10. Absorption and emission spectra of the best double QDLSC with CdSe/CdS Cu doped in the top and PbS/CdS in the bottom waveguide, illustrating the spectral overlap of $A_{top}(\lambda)$ and $E_{bottom}(\lambda)$.

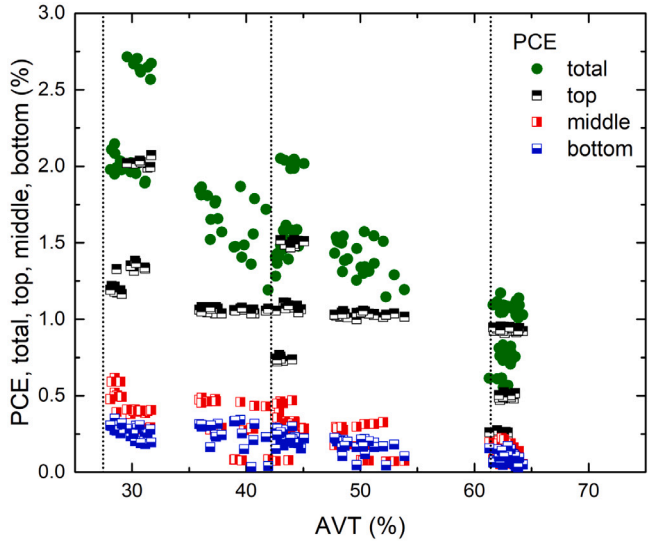

Fig. 11. PCE of triple configurations listed in Table A.1.

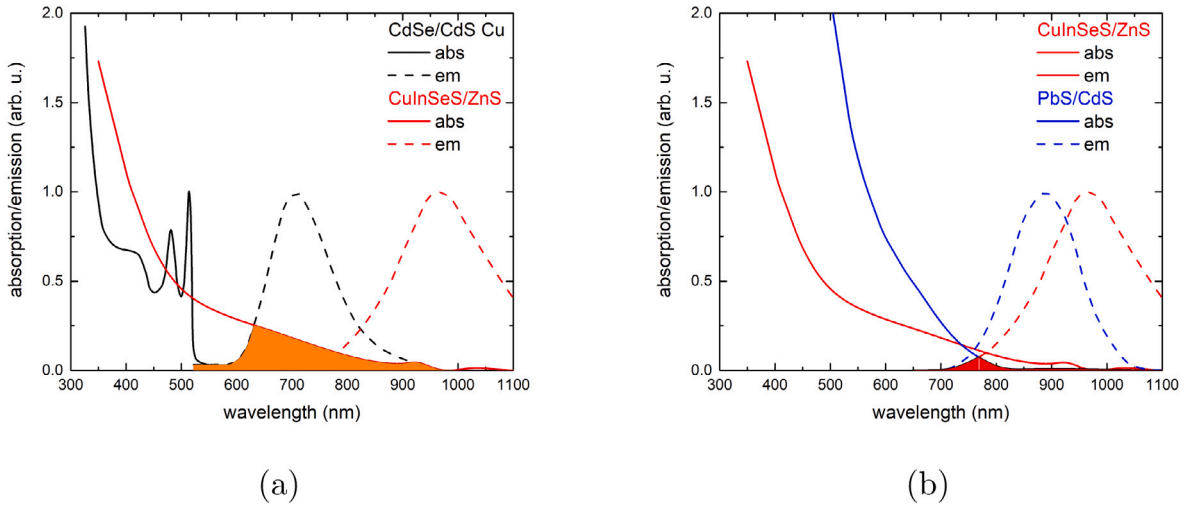

Fig. 12. Absorption and emission spectra of the best triple QDLSC with CdSe/CdS Cu doped in the top, CuInSeS/ZnS in the middle, and PbS/CdS in the bottom waveguide, illustrating the spectral overlaps between top and middle (a) and middle and bottom (b) luminophore.

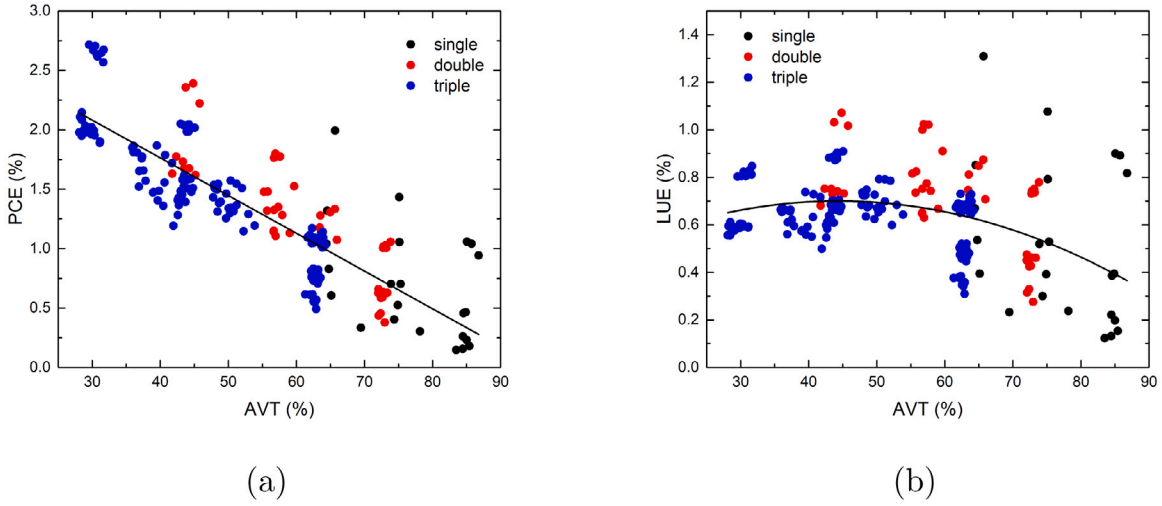

Fig. 13. (a) PCE and (b) LUE for all configurations simulated in this paper. Lines are guides to the eye.

based on eight different quantum dot luminophores. These LSC structures would serve as energy-harvesting windows. Hence average visible transmission and color rendering index are important aspects to consider. Ray trace simulations have been used to find the optimal combinations of QD luminophores, which lead to 2.7% efficiency triple configuration, using CdSe/CdS Cu doped in the top, CuInSeS/ZnS in the middle, and PbS/CdS. Higher PCE values are possible as the quantum yields used in the simulations are quite low. Future work will corroborate this.

High PCE does not necessarily mean high colorimetric quality, as many of the combinations lead to a yellow/brown color inside, behind the window, with low CRI. The LUE shows optimum values around AVT = 50%, while AVT > 70% will be required to reach good colorimetric quality.

This paper also has elaborated on the requirements for QDs when they are combined in double and triple configurations: high quantum yield and high overlap between emission spectra of luminophores in a waveguide that is on top of another waveguide and the absorption spectra of the luminophores in that waveguide.

Declaration of competing interest

The authors declare that they have no known competing financial interests or personal relationships that could have appeared to influence the work reported in this paper.

Acknowledgments

The authors would like to thank P. Moraitis for his preliminary work on the topic, providing the basis for the research, and K. Yoshikawa for sharing their data on the record efficiency PV cell. This work was supported by the Dutch Topsector Energy, The Netherlands within the framework of the MOOI-BIPVT and the TES-W projects, The Netherlands.

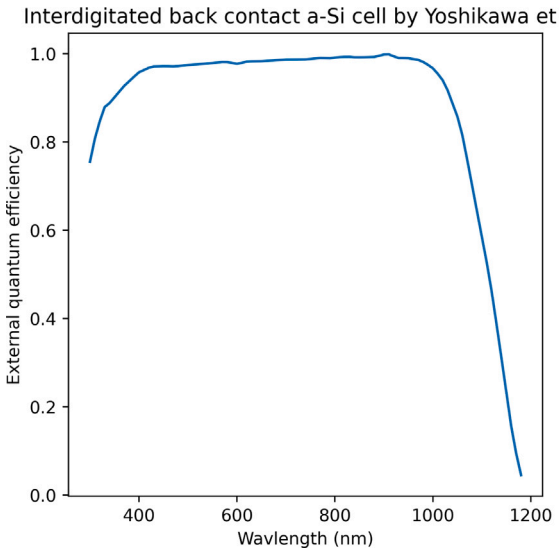

Fig. A.1. External quantum efficiency of the Si interdigitated back contact cell [49].

Appendix A

A.1. Solar cell external quantum efficiency

The external quantum efficiency as a function of wavelength of the Si interdigitated back contact cell as reported by Yoshikawa et al. [49] is shown in Fig. A.1. The diode saturation current J_s is $3 \cdot 10^{-15}$ A cm^{-2}.

A.2. Triple LSC configurations

A list of all 45 combinations for triple LSC configurations that comply with requirements stated in Section 2.5 is shown in Table A.1.

References

[1] IPCC, Global Warming of 1.5° C.An IPCC Special Report on the Impacts of Global Warming of 1.5° C Above Pre-Industrial Levels and Related Global Greenhouse Gas Emission Pathways, in the Context of Strengthening the Global Response to the Threat of Climate Change, Sustainable Development, and Efforts to Eradicate Poverty, Tech. Rep., Intergovernmental Panel on Climate Change., 2018.

[2] V. Krey, G. Luderer, L. Clarke, E. Kriegler, Getting from here to there – energy technology transformation pathways in the EMF27 scenarios, Clim. Change 123 (3–4) (2014) 369–382, http://dx.doi.org/10.1007/s10584-013-0947-5, URL http://link.springer.com/10.1007/s10584-013-0947-5.

[3] International Energy Agency, World Energy Outlook 2018, in: World Energy Outlook, OECD, 2018, http://dx.doi.org/10.1787/weo-2018-en, URL https://www.oecd-ilibrary.org/energy/world-energy-outlook-2018_weo-2018-en.

[4] F. Meinardi, F. Bruni, S. Brovelli, Luminescent solar concentrators for building-integrated photovoltaics, Nat. Rev. Mater. 2 (12) (2017) 17072, http://dx.doi.org/10.1038/natrevmats.2017.72, URL http://www.nature.com/articles/natrevmats201772.

[5] M.G. Debije, P.P.C. Verbunt, Thirty years of luminescent solar concentrator research: Solar energy for the built environment, Adv. Energy Mater. 2 (1) (2012) 12–35, http://dx.doi.org/10.1002/aenm.201100554, URL http://doi.wiley.com/10.1002/aenm.201100554.

[6] W.G.J.H.M. Van Sark, K.W.J. Barnham, L.H. Slooff, A.J. Chatten, A. Büchtemann, A. Meyer, S.J. McCormack, R. Koole, D.J. Farrell, R. Bose, E.E. Bende, A.R. Burgers, T. Budel, J. Quilitz, M. Kennedy, T. Meyer, C.D.M. Donegá, A. Meijerink, D. Vanmaekelbergh, Luminescent solar concentrators - A review of recent results, Opt. Express 16 (26) (2008) 21773–21792, http://dx.doi.org/10.1364/OE.16.021773, URL https://www.osapublishing.org/oe/abstract.cfm?uri=oe-16-26-21773.

[7] M. Ritzen, J. Houben, R. Rovers, Z. Vroon, C. Geurts, Carrying capacity based environmental impact assessment of Building Integrated Photovoltaics, Sustain. Energy Technol. Assess. 31 (2019) 212–220, http://dx.doi.org/10.1016/j.seta.2018.12.006, URL https://linkinghub.elsevier.com/retrieve/pii/S2213138818303503.

[8] T.E. Kuhn, C. Erban, M. Heinrich, J. Eisenlohr, F. Ensslen, D.H. Neuhaus, Review of technological design options for building integrated photovoltaics (BIPV), Energy Build. 231 (2021) 110381.

[9] C.J. Traverse, R. Pandey, M.C. Barr, R.R. Lunt, Emergence of highly transparent photovoltaics for distributed applications, Nat. Energy 2 (11) (2017) 849–860, http://dx.doi.org/10.1038/s41560-017-0016-9, URL http://www.nature.com/articles/s41560-017-0016-9.

[10] R. Swanson, The promise of concentrators, Prog. Photovolt., Res. Appl. 8 (1) (2000) 93–111.

[11] A. Goetzberger, W. Greubel, Solar energy conversion with fluorescent collectors, Appl. Phys. 14 (2) (1977) 123–139, http://dx.doi.org/10.1007/BF00883080, URL http://link.springer.com/10.1007/BF00883080.

[12] W.G. van Sark, Luminescent solar concentrators – A low cost photovoltaics alternative, Renew. Energy 49 (2013) 207–210, http://dx.doi.org/10.1016/j.renene.2012.01.030, URL https://linkinghub.elsevier.com/retrieve/pii/S0960148112000419.

[13] W. van Sark, P. Moraitis, C. Aalberts, M. Drent, T. Grasso, Y. L'Ortije, M. Visschers, M. Westra, R. Plas, W. Planje, The "electric mondrian" as a luminescent solar concentrator demonstrator case study, Sol. RRL 1 (3–4) (2017) 1600015, http://dx.doi.org/10.1002/solr.201600015, URL http://doi.wiley.com/10.1002/solr.201600015.

[14] B. Vishwanathan, A. Reinders, D. de Boer, L. Desmet, A. Ras, F. Zahn, M. Debije, A comparison of performance of flat and bent photovoltaic luminescent solar concentrators, Sol. Energy 112 (2015) 120–127, http://dx.doi.org/10.1016/j.solener.2014.12.001, URL https://linkinghub.elsevier.com/retrieve/pii/S0038092X14005891.

[15] A. Reinders, R. Kishore, L. Slooff, W. Eggink, Luminescent solar concentrator photovoltaic designs, Japan. J. Appl. Phys. 57 (8S3) (2018) 08RD10, http://dx.doi.org/10.7567/JJAP.57.08RD10, URL http://stacks.iop.org/1347-4065/57/i=8S3/a=08RD10?key=crossref.bfe205072ffcf62faa10e9cc15c2c72e.

[16] A. Goetzberger, Fluorescent solar energy collectors: Operating conditions with diffuse light, Appl. Phys. 16 (4) (1978) 399–404, http://dx.doi.org/10.1007/BF00885865, URL http://link.springer.com/10.1007/BF00885865.

[17] M.G. Debije, V.A. Rajkumar, Direct versus indirect illumination of a prototype luminescent solar concentrator, Sol. Energy 122 (2015) 334–340, http://dx.doi.org/10.1016/j.solener.2015.08.036, URL https://linkinghub.elsevier.com/retrieve/pii/S0038092X15004867.

[18] N. Aste, L. Tagliabue, C. Del Pero, D. Testa, R. Fusco, Performance analysis of a large-area luminescent solar concentrator module, Renew. Energy 76 (2015) 330–337, http://dx.doi.org/10.1016/j.renene.2014.11.026, URL https://linkinghub.elsevier.com/retrieve/pii/S0960148114007411.

[19] J. Roncali, Luminescent solar collectors: Quo vadis? Adv. Energy Mater. 10 (36) (2020) 2001907, http://dx.doi.org/10.1002/aenm.202001907, URL https://onlinelibrary.wiley.com/doi/10.1002/aenm.202001907.

[20] A. Anand, M.L. Zaffalon, G. Gariano, A. Camellini, M. Gandini, R. Brescia, C. Capitani, F. Bruni, V. Pinchetti, M. Zavelani-Rossi, F. Meinardi, S.A. Crooker, S. Brovelli, Evidence for the band-edge exciton of $CuInS_2$ nanocrystals enables record efficient large-area luminescent solar concentrators, Adv. Funct. Mater. 30 (4) (2020) 1906629, http://dx.doi.org/10.1002/adfm.201906629, URL https://onlinelibrary.wiley.com/doi/abs/10.1002/adfm.201906629.

[21] L.H. Slooff, E.E. Bende, A.R. Burgers, T. Budel, M. Pravettoni, R. Kenny, E.D. Dunlop, A. Büchtemann, A luminescent solar concentrator with 7.1% power conversion efficiency, Phys. Status Solidi Rapid Res. Lett. 2 (6) (2008) 257–259, http://dx.doi.org/10.1002/pssr.200802186.

[22] W. Van Sark, Will Luminescent Solar Concentrators Surpass the 10% Device Efficiency Limit?, SPIE - The International Society of Optics and Photonics, 2014.

[23] W. Van Sark, Z. Krumer, C. De Mello Donega, R. Schropp, Luminescent solar concentrators: the route to 10% efficiency, in: IEEE Xplore, IEEE, Denver, CO, USA, 2014, http://dx.doi.org/10.1109/PVSC.2014.6925380.

[24] W. Shockley, H.J. Queisser, Detailed balance limit of efficiency of *p-n* junction solar cells, J. Appl. Phys. 32 (3) (1961) 510–519, http://dx.doi.org/10.1063/1.1736034, URL http://aip.scitation.org/doi/10.1063/1.1736034.

[25] C. Yang, R.R. Lunt, Limits of visibly transparent luminescent solar concentrators, Adv. Opt. Mater. 5 (8) (2017) 1600851, http://dx.doi.org/10.1002/adom.201600851, URL http://doi.wiley.com/10.1002/adom.201600851.

[26] R.R. Lunt, Theoretical limits for visibly transparent photovoltaics, Appl. Phys. Lett. 101 (4) (2012) 043902, http://dx.doi.org/10.1063/1.4738896, URL http://aip.scitation.org/doi/10.1063/1.4738896.

[27] T.A. De Bruin, W.G.J.H.M. Van Sark, Optimising absorption in luminescent solar concentrators constraint by average visible transmission and color rendering index, Front. Phys. 10 (2022) 856799, http://dx.doi.org/10.3389/fphy.2022.856799.

[28] P. Moraitis, R. Schropp, W. van Sark, Nanoparticles for luminescent solar concentrators - A review, Opt. Mater. 84 (2018) 636–645, http://dx.doi.org/10.1016/j.optmat.2018.07.034, URL https://linkinghub.elsevier.com/retrieve/pii/S0925346718304944.

[29] Z. Krumer, S.J. Pera, R.J. van Dijk-Moes, Y. Zhao, A.F. de Brouwer, E. Groeneveld, W.G. van Sark, R.E. Schropp, C. de Mello Donegá, Tackling self-absorption in luminescent solar concentrators with type-II colloidal quantum dots, Sol. Energy Mater. Sol. Cells 111 (2013) 57–65, http://dx.doi.org/10.1016/j.solmat.2012.12.028, URL http://www.sciencedirect.com/science/article/pii/S0927024812005582.

[30] M. Rafiee, S. Chandra, H. Ahmed, S.J. McCormack, An overview of various configurations of Luminescent Solar Concentrators for photovoltaic applications, Opt. Mater. 91 (2019) 212–227, http://dx.doi.org/10.1016/j.optmat.2019.01.007, URL https://linkinghub.elsevier.com/retrieve/pii/S092534671930028X.

[31] L. Armelao, S. Quici, F. Barigelletti, G. Accorsi, G. Bottaro, M. Cavazzini, E. Tondello, Design of luminescent lanthanide complexes: From molecules to highly efficient photo-emitting materials, Coord. Chem. Rev. 254 (5–6) (2010) 487–505, http://dx.doi.org/10.1016/j.ccr.2009.07.025, URL https://linkinghub.elsevier.com/retrieve/pii/S0010854509002069.

[32] A. Chatten, K. Barnham, B. Buxton, N. Ekins-Daukes, M. Malik, A new approach to modelling quantum dot concentrators, Sol. Energy Mater. Sol. Cells 75 (3–4) (2003) 363–371, http://dx.doi.org/10.1016/S0927-0248(02)00182-4, URL https://linkinghub.elsevier.com/retrieve/pii/S0927024802001824.

[33] F. Meinardi, A. Colombo, K.A. Velizhanin, R. Simonutti, M. Lorenzon, L. Beverina, R. Viswanatha, V.I. Klimov, S. Brovelli, Large-area luminescent solar concentrators based on 'Stokes-shift-engineered' nanocrystals in a mass-polymerized PMMA matrix, Nat. Photon. 8 (5) (2014) 392–399, http://dx.doi.org/10.1038/nphoton.2014.54, URL http://www.nature.com/articles/nphoton.2014.54.

[34] F. Purcell-Milton, Y.K. Gun'ko, Quantum dots for Luminescent Solar Concentrators, J. Mater. Chem. 22 (33) (2012) 16687, http://dx.doi.org/10.1039/c2jm32366d, URL http://xlink.rsc.org/?DOI=c2jm32366d.

[35] P. Moraitis, G. Leeuwen, W. Van Sark, Visual appearance of nanocrystal-based luminescent solar concentrators, Materials 12 (6) (2019) 885, http://dx.doi.org/10.3390/ma12060885, URL https://www.mdpi.com/1996-1944/12/6/885.

[36] L. Bellia, F. Bisegna, G. Spada, Lighting in indoor environments: Visual and non-visual effects of light sources with different spectral power distributions, Build. Environ. 46 (10) (2011) 1984–1992, http://dx.doi.org/10.1016/j.buildenv.2011.04.007, URL https://linkinghub.elsevier.com/retrieve/pii/S0360132311001004.

[37] I. Knez, C. Kers, Effects of indoor lighting, gender, and age on mood and cognitive performance, Environ. Behav. 32 (6) (2000) 817–831, http://dx.doi.org/10.1177/00139160021972810, URL http://eab.sagepub.com/cgi/doi/10.1177/00139160021972810.

[38] T. Partonen, J. Lönnqvist, Bright light improves vitality and alleviates distress in healthy people, J. Affect. Disord. 57 (1–3) (2000) 55–61, http://dx.doi.org/10.1016/S0165-0327(99)00063-4, URL https://linkinghub.elsevier.com/retrieve/pii/S0165032799000634.

[39] D. Farrell, Characterising the Performance of Luminescent Solar Concentrators (Ph.D. thesis), Imperial College London, UK, 2008.

[40] D. Farrell, PVtrace, Optical ray tracing for luminescent materials and spectral converter photovoltaic devices, 2021, URL https://pypi.org/project/pvtrace/.

[41] T. Ameri, N. Li, C.J. Brabec, Highly efficient organic tandem solar cells: a follow up review, Energy Environ. Sci. 6 (8) (2013) 2390, http://dx.doi.org/10.1039/c3ee40388b, URL http://xlink.rsc.org/?DOI=c3ee40388b.

[42] M. Kennedy, Monte-Carlo Ray-Trace Modelling of Quantum Dot Solar Concentrators, Dublin Institute of Technology.

[43] M. Kennedy, S. McCormack, J. Doran, B. Norton, Modelling the effect of device geometry on concentration ratios of quantum dot solar concentrators, PV Technol. Syst. Appl. 4 (2007) 1485.

[44] A. Burgers, L. Slooff, R. Kinderman, J. Van Roosmalen, Modelling of Luminescent Solar Concentrator by Ray-Tracing, Energy Research Centre of the Netherlands.

[45] L.R. Wilson, B.C. Rowan, N. Robertson, O. Moudam, A.C. Jones, B.S. Richards, Characterization and reduction of reabsorption losses in luminescent solar concentrators, Appl. Opt. 49 (9) (2010) 1651, http://dx.doi.org/10.1364/AO.49.001651, URL https://www.osapublishing.org/abstract.cfm?URI=ao-49-9-1651.

[46] American Society for Testing and Materials (ASTM) Terrestrial Reference Spectra for Photovoltaic Performance Evaluation, Solar Spectral Irradiance: Air Mass 1.5, URL https://rredc.nrel.gov/solar//spectra/am1.5/#refs.

[47] M. Rafiee, S. Chandra, H. Ahmed, J. McCormack, Analysis of luminescent solar concentrator performance using a ray tracing algorithm: Modelling, optimization and validation, in: 13th Photovoltaic Science, Applications and Technology Conference, 2017.

[48] C. Yang, H.A. Atwater, M.A. Baldo, D. Baran, C.J. Barile, M.C. Barr, M. Bates, M.G. Bawendi, M.R. Bergren, B. Borhan, C.J. Brabec, S. Brovelli, V. Bulović, P. Ceroni, M.G. Debije, J.-M. Delgado-Sanchez, W.-J. Dong, P.M. Duxbury, R.C. Evans, S.R. Forrest, D.R. Gamelin, N.C. Giebink, X. Gong, G. Griffini, F. Guo, C.K. Herrera, A.W. Ho-Baillie, R.J. Holmes, S.-K. Hong, T. Kirchartz, B.G. Levine, H. Li, Y. Li, D. Liu, M.A. Loi, C.K. Luscombe, N.S. Makarov, F. Mateen, R. Mazzaro, H. McDaniel, M.D. McGehee, F. Meinardi, A. Menéndez-Velázquez, J. Min, D.B. Mitzi, M. Moemeni, J.H. Moon, A. Nattestad, M.K. Nazeeruddin, A.F. Nogueira, U.W. Paetzold, D.L. Patrick, A. Pucci, B.P. Rand, E. Reichmanis, B.S. Richards, J. Roncali, F. Rosei, T.W. Schmidt, F. So, C.-C. Tu, A. Vahdani, W.G. van Sark, R. Verduzco, A. Vomiero, W.W. Wong, K. Wu, H.-L. Yip, X. Zhang, H. Zhao, R.R. Lunt, Consensus statement: Standardized reporting of power-producing luminescent solar concentrator performance, Joule 6 (1) (2022) 8–15, http://dx.doi.org/10.1016/j.joule.2021.12.004, URL https://www.sciencedirect.com/science/article/pii/S2542435121005730.

[49] K. Yoshikawa, H. Kawasaki, W. Yoshida, T. Irie, K. Konishi, K. Nakano, T. Uto, D. Adachi, M. Kanematsu, H. Uzu, K. Yamamoto, Silicon heterojunction solar cell with interdigitated back contacts for a photoconversion efficiency over 26%, Nat. Energy 2 (5) (2017) 17032, http://dx.doi.org/10.1038/nenergy.2017.32, URL http://www.nature.com/articles/nenergy201732.

[50] Photon Flux | PVEducation, URL https://www.pveducation.org/pvcdrom/properties-of-sunlight/photon-flux#:~:targetText=The%20photon%20flux%20is%20defined,produced%20from%20a%20sola%20cell.

[51] M. Green, Solar cell fill factors: general graph and empirical expressions, Solid State Electron. 24 (8) (1981) 788–789.

[52] N. Aste, L.C. Tagliabue, P. Palladino, D. Testa, Integration of a luminescent solar concentrator: Effects on daylight, correlated color temperature, illuminance level and color rendering index, Sol. Energy 114 (2015) 174–182, http://dx.doi.org/10.1016/j.solener.2015.01.042, URL https://linkinghub.elsevier.com/retrieve/pii/S0038092X15000560.

[53] N. Lynn, L. Mohanty, S. Wittkopf, Color rendering properties of semi-transparent thin-film PV modules, Build. Environ. 54 (2012) 148–158, http://dx.doi.org/10.1016/j.buildenv.2012.02.010, URL https://linkinghub.elsevier.com/retrieve/pii/S0360132312000492.

[54] J. Mescher, S.W. Kettlitz, N. Christ, M.F. Klein, A. Puetz, A. Mertens, A. Colsmann, U. Lemmer, Design rules for semi-transparent organic tandem solar cells for window integration, Org. Electron. 15 (7) (2014) 1476–1480, http://dx.doi.org/10.1016/j.orgel.2014.04.011, URL https://linkinghub.elsevier.com/retrieve/pii/S1566119914001359.

[55] Commission Internationde de l'Eclairage, Commission Internationde de l'Eclairage, Publishser: Commission Internationde de l'Eclairage.

[56] N. Ohta, A.R. Robertson, Colorimetry: Fundamentals and Applications, John Wiley & Sons, Ltd, Chichester, UK, 2005, http://dx.doi.org/10.1002/0470094745, URL http://doi.wiley.com/10.1002/0470094745.

[57] R.W.G. Hunt, M. Pointer, Measuring Colour, fourth ed., in: Wiley-IS&T Series in Imaging Science and Technology, Wiley, Chichester, West Sussex, U.K, 2011, OCLC: ocn729863170.

[58] J. Schwiegerling, Society of Photo-optical Instrumentation Engineers, FieldGuide to Visual and Ophthalmic Optics, SPIE, Bellingham, Wash. (1000 20th St. Bellingham WA 98225-6705 USA), 2004, OCLC: 771367436.

[59] C. Yang, D. Liu, R.R. Lunt, How to accurately report transparent luminescent solar concentrators, Joule 3 (12) (2019) 2871–2876, http://dx.doi.org/10.1016/j.joule.2019.10.009, URL https://linkinghub.elsevier.com/retrieve/pii/S2542435119305252.

[60] N.I. Pinegin, Absolute photopic sensitivity of the eye in the ultra-violet and in the visible spectrum, Nature 154 (3920) (1944) 770, http://dx.doi.org/10.1038/154770a0, URL http://www.nature.com/articles/154770a0.

[61] Windows for High-performance Commercial Buildings, URL https://www.commercialwindows.org/vt.php.

[62] P. Fisette, Windows: Uderstanding Energy Efficient Performance, University of Massachusetts Amherst, 2003, URL https://bct.eco.umass.edu/publications/articles/windows-understanding-energy-efficient-performance/.

[63] Y. Chen, J. Vela, H. Htoon, J.L. Casson, D.J. Werder, D.A. Bussian, V.I. Klimov, J.A. Hollingsworth, "Giant" multishell cdse nanocrystal quantum dots with suppressed blinking, J. Am. Chem. Soc. 130 (15) (2008) 5026–5027, http://dx.doi.org/10.1021/ja711379k, URL https://pubs.acs.org/doi/10.1021/ja711379k.

[64] Y. Zhou, D. Benetti, Z. Fan, H. Zhao, D. Ma, A.O. Govorov, A. Vomiero, F. Rosei, Near infrared, highly efficient luminescent solar concentrators, Adv. Energy Mater. 6 (11) (2016) 1501913, http://dx.doi.org/10.1002/aenm.201501913, URL http://doi.wiley.com/10.1002/aenm.201501913.

[65] F. Meinardi, H. McDaniel, F. Carulli, A. Colombo, K.A. Velizhanin, N.S. Makarov, R. Simonutti, V.I. Klimov, S. Brovelli, Highly efficient large-area colourless luminescent solar concentrators using heavy-metal-free colloidal quantum dots, Nature Nanotechnol. 10 (10) (2015) 878–885, http://dx.doi.org/10.1038/nnano.2015.178, URL http://www.nature.com/articles/nnano.2015.178.

[66] W. Chen, J. Li, P. Liu, H. Liu, J. Xia, S. Li, D. Wang, D. Wu, W. Lu, X.W. Sun, K. Wang, Heavy metal free nanocrystals with near infrared emission applying in luminescent solar concentrator, Sol. RRL 1 (6) (2017) 1700041, http://dx.doi.org/10.1002/solr.201700041, URL http://doi.wiley.com/10.1002/solr.201700041.

[67] C.S. Erickson, L.R. Bradshaw, S. McDowall, J.D. Gilbertson, D.R. Gamelin, D.L. Patrick, Zero-reabsorption doped-nanocrystal luminescent solar concentrators, ACS Nano 8 (4) (2014) 3461–3467, http://dx.doi.org/10.1021/nn406360w, URL https://pubs.acs.org/doi/10.1021/nn406360w.

[68] M. Sharma, K. Gungor, A. Yeltik, M. Olutas, B. Guzelturk, Y. Kelestemur, T. Erdem, S. Delikanli, J.R. McBride, H.V. Demir, Near-unity emitting copper-doped colloidal semiconductor quantum wells for luminescent solar concentrators, Adv. Mater. 29 (30) (2017) 1700821, http://dx.doi.org/10.1002/adma.201700821, URL http://doi.wiley.com/10.1002/adma.201700821.

[69] F. Meinardi, S. Ehrenberg, L. Dhamo, F. Carulli, M. Mauri, F. Bruni, R. Simonutti, U. Kortshagen, S. Brovelli, Highly efficient luminescent solar concentrators based on earth-abundant indirect-bandgap silicon quantum dots, Nat. Photon. 11 (3) (2017) 177–185, http://dx.doi.org/10.1038/nphoton.2017.5, URL http://www.nature.com/articles/nphoton.2017.5.

[70] Y. Zhou, D. Benetti, X. Tong, L. Jin, Z.M. Wang, D. Ma, H. Zhao, F. Rosei, Colloidal carbon dots based highly stable luminescent solar concentrators, Nano Energy 44 (2018) 378–387, http://dx.doi.org/10.1016/j.nanoen.2017.12.017, URL https://linkinghub.elsevier.com/retrieve/pii/S2211285517307899.

[71] F. Meinardi, S. Ehrenberg, L. Dhamo, F. Carulli, M. Mauri, F. Bruni, R. Simonutti, U. Kortshagen, S. Brovelli, Highly efficient luminescent solar concentrators based on earth-abundant indirect-bandgap silicon quantum dots, Nat. Photon. 11 (3) (2017) 177–185, http://dx.doi.org/10.1038/nphoton.2017.5, URL http://www.nature.com/articles/nphoton.2017.5.

[72] K. Wu, H. Li, V.I. Klimov, Tandem luminescent solar concentrators based on engineered quantum dots, Nat. Photon. 12 (2) (2018) 105–110, http://dx.doi.org/10.1038/s41566-017-0070-7, URL http://www.nature.com/articles/s41566-017-0070-7.

[73] V.I. Klimov, T.A. Baker, J. Lim, K.A. Velizhanin, H. McDaniel, Quality factor of luminescent solar concentrators and practical concentration limits attainable with semiconductor quantum dots, ACS Photon. 3 (6) (2016) 1138–1148, http://dx.doi.org/10.1021/acsphotonics.6b00307, URL https://pubs.acs.org/doi/10.1021/acsphotonics.6b00307.